PAPER • OPEN ACCESS

Microdroplet-tin plasma sources of EUV radiation driven by solid-state-lasers (Topical Review)

View the article online for updates and enhancements.

Microdroplet-tin plasma sources of EUV radiation driven by solid-state-lasers (Topical Review)

O O Versolato[1,2,*] ![ID], **J Sheil**[1,2] ![ID], **S Witte**[1,2] ![ID], **W Ubachs**[1,2] ![ID] **and R Hoekstra**[1,3] ![ID]

[1] Advanced Research Center for Nanolithography (ARCNL), Science Park 106, 1098 XG Amsterdam, The Netherlands
[2] Department of Physics and Astronomy, and LaserLaB, Vrije Universiteit Amsterdam, De Boelelaan 1081, 1081 HV Amsterdam, The Netherlands
[3] Zernike Institute for Advanced Materials, University of Groningen, Nijenborgh 4, 9747 AG Groningen, The Netherlands

E-mail: o.versolato@arcnl.nl

CrossMark

Abstract

Plasma produced from molten-tin microdroplets generates extreme ultraviolet light for state-of-the-art nanolithography. Currently, CO_2 lasers are used to drive the plasma. In the future, solid-state mid-infrared lasers may instead be used to efficiently pump the plasma. Such laser systems have promise to be more compact, better scalable, and have higher wall-plug efficiency. In this Topical Review, we present recent findings made at the Advanced Research Center for Nanolithography (ARCNL) on using 1 and 2 μm wavelength solid-state lasers for tin target preparation and for driving hot and dense plasma. The ARCNL research ranges from advanced laser development, studies of fluid dynamic response of droplets to impact, radiation-hydrodynamics calculations of, e.g. ion 'debris', (EUV) spectroscopic studies of tin laser-produced-plasma as well as high-conversion efficiency operation of 2 μm wavelength driven plasma.

Keywords: laser-produced plasma, EUV, nanolithography, solid-state lasers, spectroscopy, tin microdroplets

(Some figures may appear in colour only in the online journal)

1. Introduction

Multiply excited states in multiply charged tin ions, bred in laser-produced transient plasma, are responsible for emitting narrow-band extreme ultraviolet (EUV) light at 13.5 nm wavelength [1] for nanolithography. EUV lithography (EUVL) has successfully entered high-volume manufacturing. EUVL enables the continued shrinking of electronic devices as captured by Moore's law. This law drives the semiconductor industry [2, 3] by postulating, or rather by demanding, that the number of transistors on an affordable CPU doubles every two years [4, 5]. The production of any semiconductor device is a repetitive opto-chemical process. Photolithography is a key step in this device manufacturing [6, 7]. It is a photochemical process in which a thin layer of material, a photoresist, is exposed to light. This light images onto the photoresist a so-called mask that is imprinted with the desired shapes, or 'features'. Photolithography is the defining step in setting the minimum obtainable feature size on a device. Following

---

* Author to whom any correspondence should be addressed.

Abbe's law of limiting resolution, the shorter the wavelength of the light used, the better the resolution. The better the resolution, the smaller the features that can be produced. EUVL, at 13.5 nm wavelength, can thus be seen as the logical, if ambitious, next step from the 193 nm light that is still used for many lithography applications. The production of the required EUV light at sufficient power, within a narrow 'in-band' 2% wavelength bandwidth centered at 13.5 nm that can be reflected by multilayer optics [8, 9], continues to present both industry and science with physics challenges, in particular in the optics and photonics fields.

Following our 2019 review [11], there are several crucial requirements for EUV light sources. Such sources should have high conversion efficiency (CE). Here, CE is defined as the ratio of in-band EUV light emitted into a half-sphere backwards towards the laser (this half-sphere being covered by the collector mirror, see figure 1) over the laser energy used to obtain it. From the perspective of sustainability, the total efficiency of converting wall-plug electricity to useful EUV light is another relevant performance indicator. Next, the amount of optics-lifetime-limiting-debris that the plasma produces (typically consisting of fragments or high-energy particles) should remain manageable. Historically, there were three promising candidate elements: Li, Sn and Xe, all of which have ions with strong electronic resonance transitions within the required bandwidth. However, for various reasons, the reported CE of Li- and Xe-based plasma sources are much lower than that of Sn-based plasmas [12, 13]. Current state-of-the-art sources of EUV light are based on the irradiation of so-called mass-limited, micrometer-sized droplets of molten tin by high-energy CO_2-laser pulses of 10.6 μm wavelength at several 10-kHz repetition rates, which creates an EUV-emitting laser-produced plasma (LPP) in several steps, see figure 1.

First, a low-energy pre-pulse deforms a spherical tin droplet into a target shape optimized for interacting with a high-energy main pulse. This deformation process involves a plethora of physical processes, ranging from laser-matter interaction, to plasma radiation-hydrodynamics, to pure fluid mechanics—with a clear separation of the relevant time scales. The ordering of these time scales determines to a large degree the overall target morphology [10, 14]. On one extreme end, short fs–ps laser pulses create bubble-like targets (see figure 1 bottom panel) as described by, e.g. Kurilovich *et al* [15] (also see [16–20]) and more recently by De Faria Pinto *et al* [21] addressing also laser polarization dependencies. On the other extreme end, long (ns) laser pulses create strongly propelled, flattened targets (see figure 1 upper panel). The industry has opted for using relatively long (∼10 ns) laser pulses, creating a quasi-stationary, strongly radiating plasma ablation front that leads to the propulsion [22–24] and the required deformation of the droplet [22, 23, 25, 26] into a 'pizza' target shape (see section 2), i.e. a relatively flat thin disk bounded by a thick rim [27, 28]. Subsequent pulses of even lower energy may be used to rarefy a tin target in order to, e.g. make a preheated plasma [29] that is later to be laser-reheated [13, 30, 31]. Vaporization of the several 10 nm thick targets [27] can also be employed to obtain further information about the thickness profile itself.
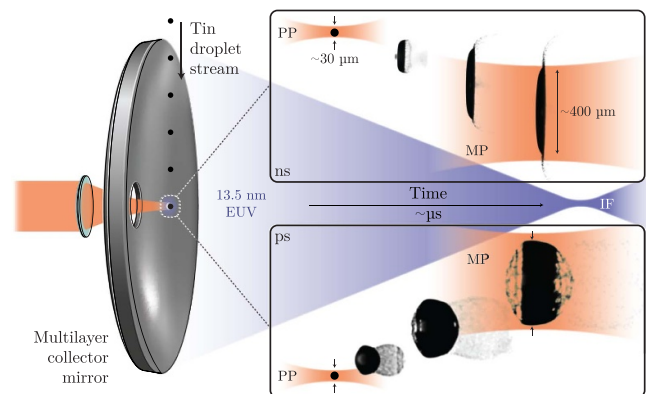

Figure 1. Schematic illustration of droplet-based EUV source operation using a pre-pulse (PP) plus main-pulse (MP) irradiation scheme including actual shadowgraph images. The top panel shows the typical deformation occurring after impact of a ns-duration pre-pulse and the lower panel the expansion following impact of a ps-duration pre-pulse. In both cases a typical desired target size is attained after several μs, at which point the target is irradiated by a more energetic main pulse, generating plasma that emits 13.5 nm EUV radiation. The EUV light is collected by the multilayer 'collector' mirror and focused at the intermediate focus (IF), the entry point of the illuminator part of an industrial wafer stepper machine. Reproduced with permission from [10].

Next, a high-energy laser main pulse drives the dense plasma from the target as prepared by the preceding pre-pulse(s). In industrial sources of EUV light the drive laser light is obtained from high-power CO_2-gas lasers operating at a wavelength of 10.6 μm [32]. Solid-state laser systems, typically operating at a shorter near-infrared wavelength could potentially provide an attractive alternative [33, 34] to the gas laser technology for driving the plasma (see section 3) with the promise of higher wall-plug efficiency and reduced complexity. Understanding the origins of the plasma-emitted EUV light, and thus the complex atomic structures of multiply charged tin ions (section 3.1) is crucial to be able to optimize future sources through predictive modeling [35]. Given the size of the outstanding challenges and the impact of new developments on society, it should not come as a surprise that modeling efforts have been stepped up worldwide. The Code Comparison session in the yearly EUV Source Workshop, organized jointly by EUV Litho, Inc. [36] and Advanced Research Center for Nanolithography (ARCNL) since 2019, has the ambition to bring together plasma modelers to improve simulation capabilities of EUV sources [35]. Besides the in-band EUV, there is interest in out-of-band (OOB) radiation in the EUV and also in the deep-ultraviolet (DUV) range. This OOB radiation may be detrimental for imaging contrast [37, 38], but can also provide a unique window into the radiative heart of the plasma motivating detailed spectroscopy efforts [39–41]. Predictive modeling should also take the expansion of the hot and dense plasma into account: ions may reach typical kinetic energies of several keV (section 3.2). The impingement of such energetic particles on nearby optical elements may be detrimental for their performance. As such, plasma expansion and the generation

(and stopping) of energetic particles is a subject of particular interest [42–47]. Producing the currently required 250 W of EUV light at the so-called intermediate focus (IF), where the source is connected to the scanner, has been a daunting, and continuing challenge. The semiconductor roadmap now asks for a stable 1000 Watt (at IF) source, quadrupling the present source performance. This calls for game-changing innovation driven by research at the fundamental level.

This topical review builds on a review from 2019 on the topic by Versolato *et al* [11], itself building on the earlier work of Banine *et al* [43] of ASML and indeed on the work of many others, e.g. of the University College Dublin (UCD) Spectroscopy Group, Lawrence Livermore National Lab (LLNL), Los Alamos National Laboratory (LANL), the Center for Materials Under eXtreme Environments (CMUXE) at Purdue University, the Institute of Spectroscopy of the Russian Academy of Sciences (ISAN), the Keldysh Institute of Applied Mathematics (KIAM), the Laboratory for Energy Conversion at ETH Zürich, the EUV Photonics Laboratory of the University of Central Florida, the Institute of Laser Engineering of Osaka University, Tokyo Metropolitan University and Gigaphoton (and still many others). This review will combine an overview of recent, relevant literature with discussions of key processes that govern the dynamics in each step in the process of generating EUV light, while focusing on recent results from the Source Department of the ARCNL in Amsterdam. ARCNL is tasked to focus on the fundamental physics and chemistry behind current and future technology for nanolithography, especially for application in the semiconductor industry.

2. Laser-droplet interaction for tin target preparation

Current high-power industrial EUV sources are based on the pulsed irradiation of a high-frequency stream of micrometer-sized droplets of molten tin. The reason for using individual, well-separated droplets is that each droplet serves as an isolated reservoir of tin with limited mass. Such mass-limited targets enable careful optimization of CE while using a minimum amount of tin and, moreover, generate a minimal amount of debris. The careful shaping of a spherical droplet into a shape optimally suited for interaction with the energetic main pulse is key for such careful optimization and control.

The transformation of a spherical tin droplet into a suitable target using laser 'pre-pulses' involves a broad range of physical processes. Of key importance for the final morphology of the target is the ordering of the time scales associated with the various physical processes. Among the shortest timescales is the electron-ion relaxation time $\tau_{e-i} \sim 10$ ps, which is related to the exchange of energy between electron and ion subsystems, with the electron subsystem directly heated by the laser pulse through the process of inverse brehmsstrahlung.

The next longest time scale is the plasma-hydrodynamic time scale, which is set by the ratio of the plasma flow length scale distance to the velocity of this flow. This flow length scale, i.e. the distance between droplet and critical surface

(where the plasma electron density equals the critical density for the incoming laser beam) is of order ~ 10 μm and the typical flow velocity is given by the speed of sound in the laser produced plasma corona $\sim 10^5$ m s^{-1} [48]. Together they yield a hydrodynamic time scale $\tau_h \sim 100$ ps [48]. Next is the acoustic time scale of the tin liquid τ_a on which pressure waves, launched by the plasma produced by the laser pulse, acoustically travel (with sound speed $c \sim 2500$ m s^{-1}) through the droplet (with radius $R_0 \sim 25$ μm), $\tau_a \sim R_0/c \sim 10$ ns. This time scale is followed by the inertial time scale $\tau_i = R_0/U \sim$ 100–1000 ns on which the droplet relevantly deforms. Following the practice well-established in the fluid dynamics literature, the typical deformation velocity is here taken to be the propulsion, or impact velocity $U \sim 100$ m s^{-1}. This impact velocity should be compared to the more relevant velocity $\dot{R}_0$, the initial radial expansion rate. Typically $\dot{R}_0 \sim U$, however the precise relation depends on, e.g. how tightly the laser is focused onto the droplet. More tightly focused beams lead to larger $\dot{R}_0$ (and $\dot{R}_0 > U$). Hernandez-Rueda *et al* [49] have explored a large parameter space to investigate the influence of the tin droplet diameter as well as the laser beam diameter and energy on the $\dot{R}_0/U$ ratio. Next, they compared the experimental U and $\dot{R}_0$ values to those obtained with detailed radiation-hydrodynamic simulations using the RALEF-2D code which in turn enabled validating analytical fluid-dynamics modeling [26].

The near-equivalence $\dot{R}_0 \sim U$ may break down if the laser pulse is of particularly short duration ($\dot{R}_0 \gg U$ with $U \approx 0$, cf figure 1).

Last in line is the capillary time scale $\tau_c = \sqrt{\rho R_0^3/\sigma} \sim$ 10 μs, with liquid density ρ and surface tension σ [26]. This is the time scale on which retraction of the sheet due to surface tension occurs. Theoretical work by Reijers *et al* [14], recently experimentally validated by Meijer *et al* [10], made clear that the time scale of significant changes in laser intensity (typically of the order of the laser pulse duration τ_p) over the time scale ordering $\tau_{e-i} < \tau_h < \tau_a < \tau_i < \tau_c$ is a crucial factor determining the fluid-dynamic deformation of the droplet and final target morphology.

From the whole palette of pre-pulse settings, the EUVL industry hamicros opted for using relatively long ($\tau_p \sim 10$ ns) laser pulses which, given that $\tau_p \gg \tau_h$ [48], create a quasi-stationary plasma that leads to the propulsion and the required deformation of the droplet into a relatively flat, thin disk bounded by a thick rim. This 'pizza' shape was uncovered and experimentally mapped in detail by Liu *et al* [28], who studied the morphology of a radially expanding sheet of liquid tin formed by ns-pulse Nd:YAG laser impact on a spherical microdroplet. Specifically, the sheet thickness profile and its time evolution were captured over a range of laser-pulse energies for two droplet sizes. Two complementary methods were employed to determine the thickness profile. In the first method, the finite transmissivity of the several 10 nm thick stretched liquid-metal sheet was recorded and, with the known optical constants of tin [50], the transmissivity could be converted to a local thickness $h(r)$ as a function of the radial coordinate r (see figures 2(a1.2) and (a2.2)). In the second
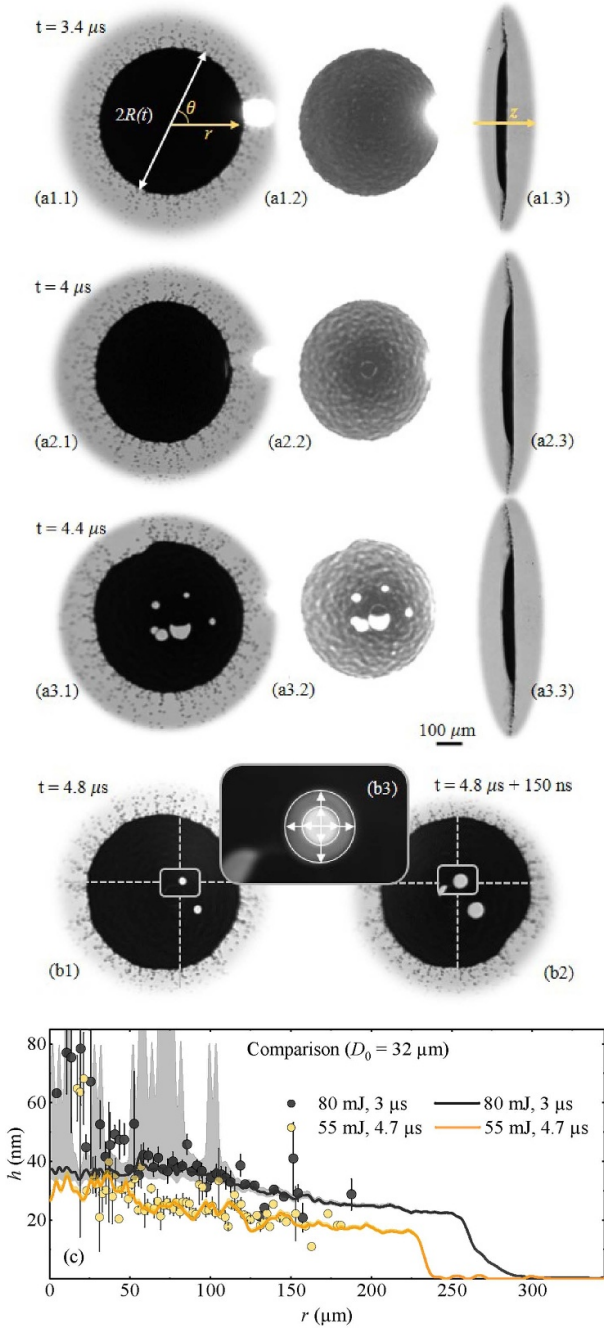
Figure 3. Volume ratio of the sheet to that of the initial droplet V_{sheet}/V_0 as a function of non-dimensional time t/τ_c for various droplet sizes and Weber numbers (see [28]). Brown data (circles) are obtained from [28] using the method illustrated in figure 2. Dark gray data (squares) are obtained from a laser vaporization method [27]. The analytical prediction for V_{sheet}/V_0 is presented as a black solid line. The inferred volume ratios V_{rim}/V_0 and V_{fragment}/V_0 are presented as blue and red lines, respectively, following [28]. The vertical line marks $t/\tau_c \approx 0.55$ from where the model validity is unclear. Figure data taken from [27, 28].

Figure 2. Shadowgraph images of expanding sheets from tin microdroplets hit by a Nd:YAG ns laser pulse at 1.064 μm. ((a1.1), (a2.1), (a3.1)) Front views of liquid sheets at time delay t (laser impacts at $t = 0$). The bright spot visible in several of the images is from plasma emission. ((a1.2), (a2.2), (a3.2)) Same images with a digitally modified contrast. ((a1.3), (a2.3), (a3.3)) Corresponding side-view images (laser impacts from the left, propelling the droplet to the right). In ((a1.1), (a1.3)), the cylindrical coordinate system (r, θ, z) with its origin at the center of sheet is depicted. At later times, holes appear cf ((a3), (b1), (b2)). The overlay of a hole is highlighted by a white box in both ((b1), (b2)). The arrows in inset (b3) indicate the receding edge of the hole the velocity of which gives the local thickness (see main text). (c) Sheet thickness as a function of the radial coordinate. Comparison of results obtained using a backlight-transmission method (cf panel (a2.2)) and from a complementary method using hole-opening velocities (cf panels (b1) and (b2)). Reproduced from [28]. CC BY 4.0.
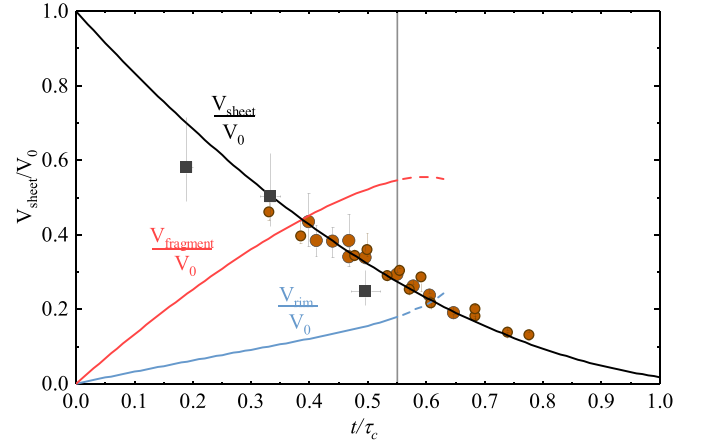
method, the speed of opening of spontaneously formed holes (cf figures 2(b1)–(b3)) in the stretching sheet is experimentally measured, which again allows one to obtain $h(r)$ following Culick [51]. Results from the two methods, indicating the presence of a thin tin sheet just several 10 nm in thickness, were shown to be in excellent agreement cf figure 2(c). Moreover, all obtained thickness profiles were shown to collapse onto a single self-similar curve enabling the prediction of the thickness profile under a wide range of experimental conditions.

Spatial integration of the thickness profiles enables one to determine the volume of the sheet as a function of time after pre-pulse laser impact, see figure 3. Remarkably, less than half of the initial amount of tin remains in the sheet under these conditions. Further analysis shows that the largest fraction of the mass lost from the sheet during its expansion ends up as fine fragments (see figure 3). Liu *et al* [28] proposed that such mass loss can be minimized by producing the sheet targets on the shortest possible timescales. A follow-up study validated this proposal, where Liu *et al* [27] irradiated thin tin sheets with a low-intensity laser pulse. This auxiliary pulse, used as a probe with an intensity below plasma threshold (following Meijer *et al* [52]), induced vaporization which enabled investigation of the thickness profile of the sheet and its mass also at earlier times (see figure 3). The results demonstrated that increasing the energy of the Nd:YAG laser pulse, which enabled reaching the predetermined target radius more quickly, resulted in a larger mass fraction remaining in the sheet. As a corollary, less tin ended up in other channels of the mass distribution such as fragments surrounding the sheet, thus leaving more mass in the target sheet available for interaction with the more energetic main laser pulse to produce EUV light.

3. Main pulse: using solid-state lasers to drive EUV emission

Once a suitable target shape is reached, the main laser pulse transforms the liquid target into a hot and dense EUV emitting plasma [11, 73]. In the industry, the laser providing these pulses currently is an infrared 10.6 μm wavelength CO_2 gas laser. Tin plasma driven at this laser wavelength has particularly high CE (see figure 4). Solid-state lasers, typically operating at shorter, near-infrared wavelengths may soon be able to provide a viable alternative to these CO_2 gas lasers [74]. Such solid-state laser systems may be more compact and have higher wall-plug efficiencies. Reducing the drive laser wavelength from 10.6 μm will, however, also increase the typical tin ion densities in the region where EUV light is generated in the plasma. This effect can be qualitatively understood [11] from the increase in critical electron density n_c with decreasing drive laser wavelength λ through $n_c \sim \lambda^{-2}$. Beyond n_c, where the electron plasma frequency is equal to the laser light frequency, laser light cannot propagate. Relevant plasma densities increase at a slower pace $\sim \lambda^{-1}$ [72] (see below), but nevertheless the plasma gets more dense with decreasing drive laser wavelength. Increased plasma density is associated with larger optical depths (the product of atomic opacity, mass density, and path length [72, 75]), which causes opacity broadening of the 13.5 nm emission feature beyond the 2% acceptance bandwidth, thus reducing the spectral purity (SP, defined as the ratio of spectral energy in a 2% bandwidth around 13.5 nm to the total EUV energy) and with it the maximally obtainable CE [55, 61, 63, 65, 71, 75–77].

Nishihara *et al* [12] provided simulation results for optimal drive laser intensities, with predictions for obtainable CE for idealized '0D' plasmas. In figure 4(a), CE values from the simulations are indeed shown to increase with increasing drive laser wavelength. The optimum laser intensity decreases with increasing laser wavelength (and, thus, with decreasing plasma density). Several recent simulation efforts (see, e.g. [33]) have drawn the attention of the EUV source community to the use of a 2 μm drive laser, further supported by the recent introduction of novel concepts for high-power solid-state laser systems operating at this wavelength. Such promising simulations are particularly challenging, not least because of the complex atomic physics involved, and require experimental benchmarks.

Schupp *et al* [72, 78] and Behnke *et al* [34] recently reported the first experimental study of 2 μm laser-driven tin plasmas. These studies, discussed in section 3.3, confirmed the simulation results with regards to the particular promise of the 2 μm driver. Additional experiments are required in unison with detailed predictive modeling efforts. The modeling efforts need as input accurate atomic physics data to enable understanding the origins of the plasma-emitted EUV light. These origins, discussed in section 3.1, were recently shown to be much more complex than previously thought. Predictive modeling should also take into account the expansion of the hot and dense laser-driven plasma, where ions reach kinetic energies on the order of several keV. This topic will be discussed further in section 3.2. The development of advanced
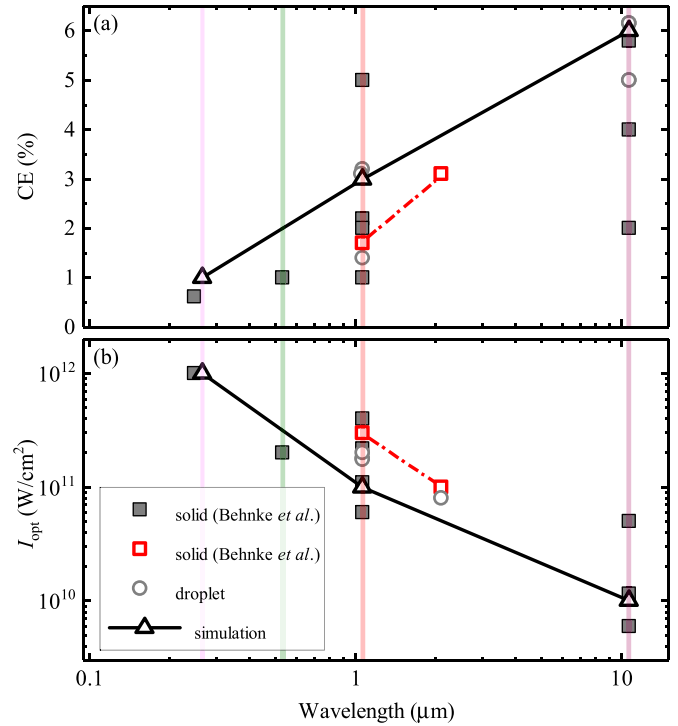

Figure 4. (a) Conversion efficiency (CE) and (b) optimum laser intensity (I_{opt}) values as a function of drive laser wavelength as obtained from previous experiments on planar solid (full gray squares) and droplet (open gray circles) tin targets (data from [53–72]). Overlapping data points are shifted vertically for visibility. Simulation results [12] for plasma under optimal conditions are shown (open black triangles) connected by straight lines. The vertical lines, moving from right to left, indicate the wavelengths of CO_2 laser light, Nd:YAG laser light (fundamental), as well as the second and fourth harmonics of Nd:YAG laser light. The results of the work of Behnke *et al* [34] are shown as open red squares (see main text). Adapted with permission from [34]. © The optical Society.

solid-state laser systems at ARCNL will enable dedicated studies to find the true optimum conditions to drive tomorrow's plasma sources of EUV light, as we conclude in section 4.

3.1. Strong contributions of multiply excited states to EUV emission

The complex electronic structures of multiply charged tin (Sn) ions are the root cause of their particular attractiveness for use in next-generation nanolithography [3, 11, 32, 43, 70, 79, 80]. They are employed as emitters of in-band 13.5 nm EUV photons. The suitability of Sn ions for this application stems from their open-4d-subshell structures [39, 81–90]. Within these structures, $\Delta n = 0$ one-electron-excited configurations are well-known to decay to the ground state manifold via a multitude of transitions clustered together in unresolved transition arrays (UTAs) [91] centered around 13.5 nm. An exceptional feature of Sn ions is the fact that the average excitation energies of these configurations are similar across the isonuclear sequence Sn^{11+}–Sn^{14+}, making these charge states excellent radiators of 13.5 nm light. Recently, however, a team of
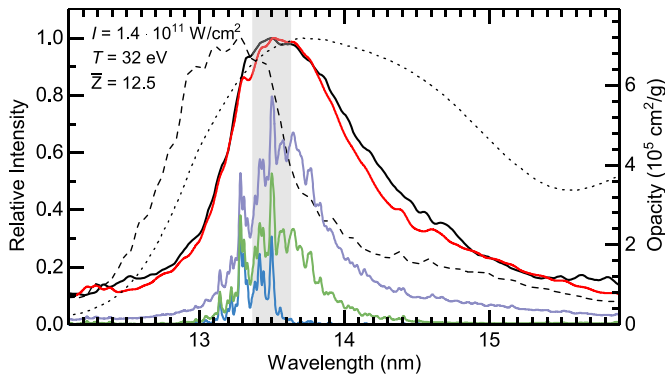
Figure 5. Comparison of atomic opacity calculations with an experimental spectrum using a 1D radiation transport through a single-density (0.002 g cm^{-3}), single-temperature plasma (32 eV)—see main text. Experimental spectrum (black solid line; plasma generated by 1.064-μm, 15-ns pulse laser impact on a tin droplet at 1.4×10^{11}W cm^{-2} intensity) and calculated flux (red solid line) are shown, normalized to their respective maxima. The dashed and dotted lines show the spectral fluxes calculated from the opacity spectrum reported in [89] and HULLAC calculations [76], respectively. The individual contributions to the opacity spectra are also shown. The mean charge state of the calculated plasma is $\bar{Z} = 12.5$. The grey area highlights the industrially-relevant 2% bandwidth centered at 13.5 nm. Reproduced from [1]. CC BY 4.0.

researchers from ARCNL and Los Alamos National Laboratory (LANL) found that the characteristics of Sn ions are even more special and that the EUV light generated in these plasmas originates predominantly from transitions from multiply excited states [1]. Contrary to the prevailing view, contributions from one-electron-excited states are not the prime sources of EUV light in the in-band spectral region. This serendipitous alignment of transitions in singly, doubly, and triply excited systems occurs over a range of charge states Sn^{11+}–Sn^{14+}. The work [1] revealed the doubly magic behavior of tin and the origins of the EUV light.

The importance of the multiply excited states for the EUV emission is demonstrated in figure 5, where a comparison between an experimental emission spectrum (black curve, produced from plasma generated by impinging a Nd:YAG laser pulse onto a tin microdroplet) and the spectral flux obtained from one-dimensional radiation-transport modeling (red curve, which uses as input the ATOMIC opacity calculations) is shown [1]. The spectral flux calculated using a single-density, single-temperature approach clearly reproduces the measured emission strikingly well. Without the contributions from the multiply excited states, it would clearly not be possible to explain the experimental spectrum to any degree of satisfaction. To further highlight the importance of these transitions, as well as the accuracy of the work of Torretti *et al* [1], the results are compared with calculations from previous works [76, 89].

In follow-up work by Sheil *et al* [92], the Los Alamos ATOMIC code was used to investigate the spectral contribution from transitions from multiply excited states in CO$_2$ laser-driven ($\lambda = 10.6$ μm) tin plasma conditions. Here, in comparison the Nd:YAG drive laser case, much lower plasma densities are obtained where local-thermodynamic equilibrium (LTE)

conditions are not met. Busquet's [93] ionisation temperature method was employed to match the average charge state of a non-local-thermodynamic equilibrium (non-LTE) plasma with an LTE one, establishing a so-called ionization temperature T_Z. This approach is found to generate LTE-computed configuration populations in excellent agreement with the non-LTE populations. A corollary of this observation is that the non-LTE populations are well-described by Boltzmann-like exponential distributions characterized by the effective temperature T_Z. Subsequently, extensive level-resolved LTE opacity calculations were performed at T_Z. Sheil *et al* [92] also found that the leading contributions to the opacity near 13.5 nm arise from transitions from multiply excited states. These results reinforce the need to include multiply excited states in atomic models from which the radiative properties of laser-driven tin plasmas are generated. The work of Sheil *et al* [92] paves the way for the generation of detailed LTE opacity tables at non-LTE plasma conditions, which can be incorporated in radiation-hydrodynamic simulations of laser-driven tin plasmas. Such simulations will enable reliable predictions of EUV emission from LPPs and will play a key role in guiding experimental efforts in the characterization and optimization of laser-driven plasma sources of EUV light.

Aside from the in-band EUV radiation, spectroscopy in other wavelength ranges can provide further valuable insight into the properties of the laser-driven tin plasma. Indeed, detailed information about the contribution of the various charge states to the main 13.5 nm emission feature can be obtained from OOB transitions. Short-wavelength emission, located between 7 and 12 nm, enables the assessment of the charge state distribution [39, 40] and served to diagnose industrial CO$_2$-laser-driven plasmas as demonstrated by Torretti *et al* [41]. Using the method developed by Scheers *et al* [94] for charge-state-resolved spectroscopy, Bouza *et al* [95] compared laser-driven plasma emission with electron beam ion trap spectroscopies at longer EUV wavelengths. This plasma spectroscopy work was later extended to include DUV and UV wavelengths, where an intensity-calibrated spectrum from 5 all the way up to 265 nm wavelength [96] was recorded using a novel transmission grating spectrometer (TGS) developed by the MESA+ XUV Optics group at Twente University, in tandem with a smart choice of filters. The TGS will soon be upgraded with one-dimensional imaging capabilities, enabling space-resolved characterization of plasma ionicity (see Byers *et al* [97]). Scheers *et al* investigated the UV and optical emission from the lower charge states in the plasma [98]. This work was followed by a temporally and spatially resolved study of the optical emission from these lower charge states, where the evolution of electron density and temperature in the 'afterglow' of the LPP was quantified using a fiber-coupled imaging spectrometer [99]. Further spectroscopic studies will undoubtedly drive predictive modeling efforts and the development of future EUV light sources.

3.2. Plasma expansion—'fast ionic' debris

Besides the sought-after EUV light, a laser-produced plasma produces debris in the form of fast ions, the impact of which
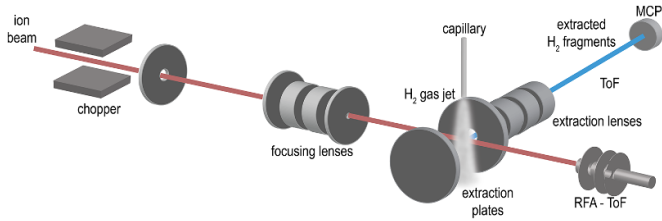
Figure 6. Schematic view of the crossed-beam setup that will be used to measure charge exchange and energy loss in the forward-scattering direction by means of a combined electrostatic Time-of-Flight analyzer system, while target fragments from the interactions of Sn^{q+} ions colliding with H_2 are extracted sideways into a Time-of-Flight spectrometer. The full setup can be operated on high voltage to decelerate the incoming ion beams allowing for a coverage of the full kinetic energy range of plasma ions from close to 0 to tens of keV.

Figure 7. The distribution of the number of ions over ion kinetic energy. The experimental ion energy distribution is shown in red (solid curve) and the RALEF-2D ion energy distribution is shown in black (solid curve). Also illustrated in green are the predictions of analytic models of plasma expansion (see discussion in [106]). Reproduced from [106]. © The Author(s). Published by IOP Publishing Ltd. CC BY 4.0.

may limit the lifetime of the light collecting multilayer optics. Rai *et al* [100] studied single-collision scattering of keV-energy ions off surfaces to elucidate the absence of a single-scattering peak in the here relevant Sn-Ru collisions [101] and to test the predictive power of standard Monte Carlo binary collision codes such as SRIM (Stopping and Range of Ions in Matter) [102]. These codes, which were primarily developed for modeling swift particle interactions with solid state targets, are also used to simulate the stopping and mitigation of plasma ions in hydrogen buffer gas surrounding the plasma. Corresponding experimental data on slow ($E \leqslant 100$ eV amu^{-1}) heavy ions is by and large lacking. To investigate the interactions between Sn^{q+} ions with H_2 we have commissioned an advanced crossed-beam type setup based on experience from previous crossed-beam experiments [103, 104], see figure 6.

Fast plasma ions are generated during the expansion phase of the plasma [105]. Understanding such plasma expansion at the fundamental level is key for modeling the laser-produced plasma. Hemminga *et al* [106] presented the results of a joint experimental and theoretical study of plasma expansion driven by Nd:YAG laser ablation (laser wavelength $\lambda = 1.064$ μm) of tin microdroplets under conditions relevant for nanolithography. The experimental measurements indicate a near-plateau in the ion energy distribution for kinetic energies in the 0.03–1 keV range, a peak near 2 keV followed by a sharp fall-off in the distribution for energies above 2 keV (red curve in figure 7). Charge-state resolved measurements, performed with a cross-calibrated electrostatic analyzer in time-of-flight mode (ESA-ToF) [107], attributed this peaked feature at 2 keV to the existence of peaks (centered near 2 keV) in the Sn^{3+} − Sn^{8+} ion energy distributions. To understand the physical origin of this peaked feature, Hemminga *et al* [106] performed two-dimensional simulations of the plasma initiation, growth and subsequent expansion using the radiation hydrodynamic code RALEF-2D. As is evident from figure 7, excellent agreement was found between the simulated ion energy distribution and the measurements both in terms of the shape of the distribution and the absolute number of detected ions. The peak in the ion energy distribution near 2 keV was attributed to a
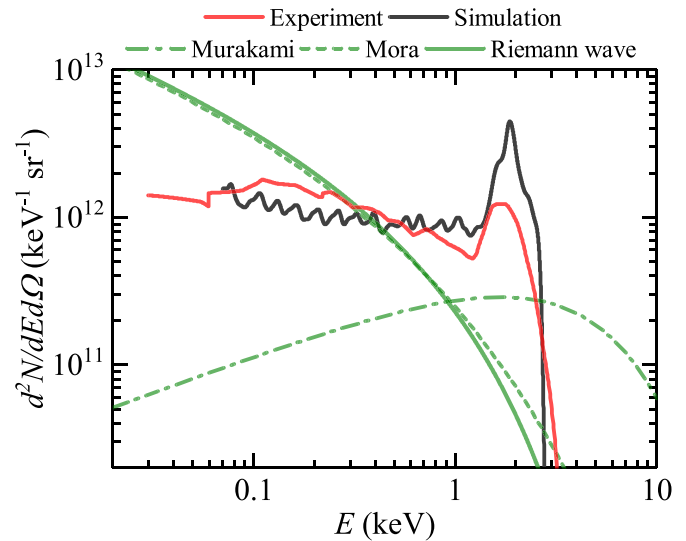
quasi-spherical expanding shell formed at early times in the expansion.

These results demonstrate that the single-fluid single-temperature approach implemented in RALEF-2D can not only reproduce the general shape of the experimental ion energy distribution, but it can also provide a reliable prediction for the absolute number of ions, thus paving the way for future predictive modeling of plasma EUV light sources.

3.3. Comparing plasmas driven by 1 and 2 μm wavelength lasers

Recent simulation efforts at Lawrence Livermore National Laboratory (LLNL, and see, e.g. [33]) have indicated that use of a drive laser at $\sim$2 μm wavelength may be particularly beneficial for driving the tin plasma. Concurrently, LLNL introduced the concept of high-energy, high-power Big Aperture Thulium (BAT) laser systems operating at 1.9 μm wavelength.

At ARCNL, experiments were started to investigate the potential of such novel lasers and novel wavelengths to drive plasma. Behnke *et al* [34] were the first to present an experimental study of a 2 μm laser-driven tin plasma in which a planar tin target was irradiated with laser pulses of 5 ns duration. The 2 μm laser light source (cf figure 8(a) inset) used comprised a potassium titanyl phosphate (KTP) based master oscillator power amplifier (MOPA) operated in type-2 phase matching. The MOPA is pumped at a 10 Hz repetition rate by a seeded, Q-switched Nd:YAG laser providing pulses of 10 ns duration. First, a 2170 nm idler seed beam is created in a singly-resonant optical parametric oscillator (OPO). To create the seed beam, a fraction of the pump light is demagnified to a beam diameter of 1.5 mm and is coupled into the
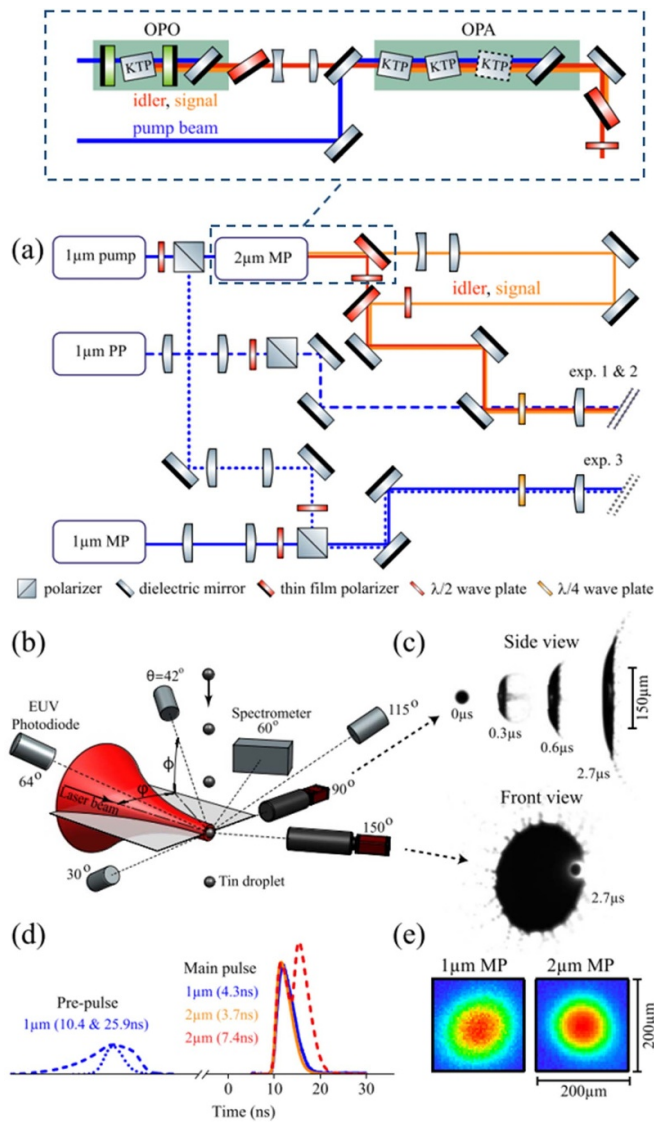
Figure 8. (a) Schematic representation of the laser beam setups adopted in the experiments described in Schupp *et al* [78] using a pre-pulse (PP) to predeform droplet targets before impact of the main pulse (MP) lasers. The top inset, taken from [72], shows a master oscillator power amplifier (MOPA) setup (see main text). (b) Continuation from (a) showing the locations and angles of the various detectors. (c) Selection of front- and side-view shadowgraphs of the tin targets used for plasma generation, recorded by the two cameras indicated in (b). (d) Temporal and (e) spatial profiles of the laser beams. (Upper panel) Reproduced from [72]. CC BY 4.0. (Lower panels) Reproduced from [78]. © The Author(s). Published by IOP Publishing Ltd. CC BY 4.0.

OPO, operated in a collinear alignment. About 20% of the pump radiation is converted into a 2090 nm wavelength signal beam and a 2170 nm idler beam. A dichroic mirror separates the signal and idler beams from the partially depleted pump. The idler beam is subsequently expanded to 11 mm in diameter to seed the optical parametric amplifier (OPA), while the signal beam is removed through polarization optics. The OPO and OPA are pumped by the same laser. For pumping the OPA, 1.3 J of the Nd:YAG laser light is delayed by 1.3 ns and is reduced to a beam size of 10 mm in diameter.

Seed and pump beams are overlapped on a dichroic mirror after which they pass several 18 mm long KTP crystals. The crystal orientation is alternated to compensate for walk-off. A total (sum + idler) energy of several 100 mJ can routinely be achieved. Pump and signal beams are separated from the idler using a dichroic mirror and polarization optics, respectively. To adjust the energy of the idler beam, a waveplate/ polarizer combination is employed before focusing the beam onto the target. The size of the focal spot was approximately $100 \times 100 \ \mu m^2$. Spectroscopic investigations were performed for plasmas driven by this 2 μm wavelength pulsed laser light and comparisons were made with plasmas driven by the 1 μm pump laser light at several laser intensities. Very similar EUV spectra, and thus underlying plasma ionicities, were obtained when the intensity ratio was kept fixed at $I_{1\,\mu m}/I_{2\,\mu m} = 2.4(7)$. Crucially, the CE was found to be a factor of two larger (at the given 60 degree observation angle) for the 2 μm laser-driven plasma compared to the case of the denser, 1 μm driven plasma.

Following soon after, Schupp *et al* [72] presented experimental spectroscopic studies of EUV light emitted from plasma produced by the irradiation of tin microdroplets with 5 ns pulsed, 2 μm wavelength laser light (cf figure 8) using the same laser system as in [34]. Emission spectra were compared to those obtained from plasma driven by 1 μm wavelength Nd:YAG laser light over a range of laser intensities. Over the studied range of drive laser intensities, it was found that similar spectra (and thus underlying plasma charge state distributions) were obtained when the ratio of the 1–2 μm laser intensities was fixed at a constant value, in good agreement with the findings of Behnke *et al* [34]. Schupp *et al* [72] also performed laser-plasma simulations using the radiation-hydrodynamic code RALEF-2D and found good agreement regarding the intensity ratio. Their experimental findings, supported by the simulations, indicate an approximately inversely proportional scaling $\sim \lambda^{-1}$ of the relevant plasma electron density and the aforementioned required drive laser intensities with drive laser wavelength λ in line with the predictions of Nishihara *et al* [12] (cf figure 4) for a plasma system of much reduced complexity. The $\sim \lambda^{-1}$ scaling was also found to extend to the optical depth as captured in the observed changes in spectra over a range of droplet diameters. The decrease of optical depth with increasing drive laser wavelength is illustrated in figure 9, where experimental spectra from 1, 2, and 10 μm drivers are seen to decrease in width with increasing λ.

In a detailed follow-up work, Schupp *et al* [78] reported on the EUV emission properties of tin plasmas produced by the irradiation of pre-pulse-preformed liquid tin targets by 2 μm wavelength laser pulses (cf figure 8). In a two-pulse scheme, much like in the current industrial setting, a pre-pulse laser is first used to deform tin microdroplets into thin, extended disks (cf figure 8(c)) before the main (2 μm) pulse creates the EUV-emitting plasma. The effects of a change in 2 μm drive laser intensity and laser pulse duration (3.7–7.4 ns; for the longer pulses, both signal and idler were used) were studied. It was found that the angular dependence of the emission of light within a 2% bandwidth around 13.5 nm and within
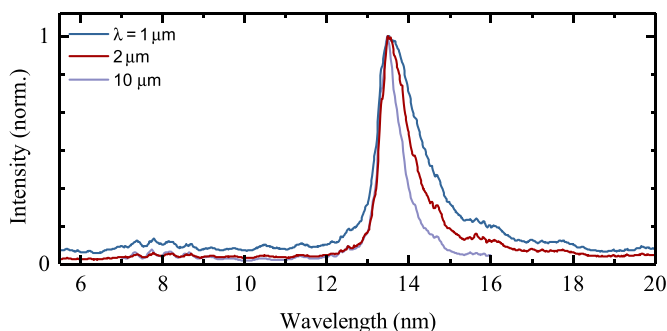
Figure 9. EUV spectrum produced with a 2 μm laser-driven tin plasma (red line) compared to that obtained from a 1 μm laser-driven plasma (blue line) at intensities of 1.1 and 2.4 $\times$ 10^{11} W cm^{-2}, respectively. Also shown is a spectrum obtained using a 10 μm CO$_2$ laser that here represents the case of small optical depth (reproduced from [108] in [72]). Reproduced from [72]. CC BY 4.0.
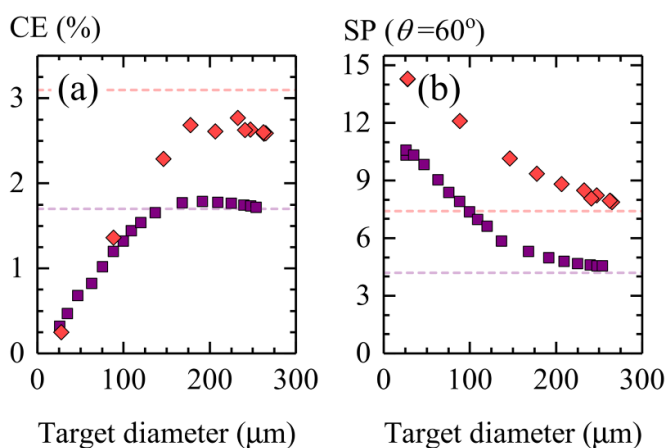

Figure 10. Comparison of results for drive laser beams of 1 (solid purple squares) and 2 μm (solid orange diamonds) wavelength at intensities of 1.9 and 1.0 $\times$ 10^{11} W cm^{-2}, respectively. (a) CE and (b) SP as a function of target diameter. The dashed lines in (a) and (b) indicate the CE and SP values obtained from laser-irradiated, planar-solid tin targets, respectively [34]. All SP values provided are calculated with respect to the measured spectral range of 5.5–25.5 nm. Reproduced from [78]. © The Author(s). Published by IOP Publishing Ltd. CC BY 4.0.

the backward 2π hemisphere around the incoming laser beam is almost independent of intensity and duration of the 2 μm drive laser. With increasing target diameter, the emission in this 2% bandwidth becomes increasingly anisotropic, with a greater fraction of light being emitted into the backward 2π hemisphere around the incoming laser beam. For direct comparison, a similar set of experiments was performed with a 1 μm wavelength drive laser. EUV emission spectra were found to exhibit prominent self-absorption of light around 13.5 nm in the 1 μm case, while in the 2 μm case only a modest opacity-related broadening of the spectral feature at 13.5 nm was observed. The work demonstrated the enhanced capabilities and performance of 2 μm driven plasmas produced from disk targets when compared to 1 μm driven plasmas both in terms of CE (cf figure 10(a)) and SP (cf figure 10(b)).

The significant improvement of the spectral performance of the 2 μm vs 1 μm driven plasma provides strong motivation for the development of high-power, high-energy near-infrared lasers to enable the development of more efficient and powerful sources of EUV light. Such solid-state lasers may soon become a viable alternative given the fact that solid state lasers are more compact, are more flexible, and are expected to be more stable than presently used CO$_2$-gas lasers. Moreover, solid-state lasers are expected to have a significantly higher efficiency in converting electrical power to laser light, thus enabling obtaining a higher overall efficiency converting wall-plug electrical power to useful in-band EUV radiation. The optimum laser wavelength of such a solid-state drive laser, operating under realistic conditions, is however still unclear. At ARCNL, we are developing advanced high-energy, low-repetition rate laser systems [109], flexible in both wavelength (1–4 μm) and spatiotemporal beam profile. These laser systems will be employed to drive microdroplet tin plasma to produce EUV light under industrially relevant conditions, facilitating the design of the ultimate laser-driven plasma source of EUV light to drive tomorrow's nanolithography.

4. Conclusions

In this topical review in the JOPT special issue on Advances in Optics in The Netherlands, key physics aspects of laser-driven tin plasmas are discussed. Such plasmas are the source of extreme ultraviolet light at 13.5 nm wavelength for state-of-the-art nanolithography. Generating ever-more EUV light at ever-increasing efficiencies and machine up-times provides a challenge to both science and industry. This is especially true in the context of a 1000 W EUV source, which now lies on the horizon of the semiconductor roadmap (such a source would quadruple the present source performance). In this review, we combine an overview of selected literature, focusing on recent results from the Advanced Research Center for Nanolithography (ARCNL) in Amsterdam. ARCNL is tasked to focus on the fundamental physics and chemistry underpinning current and future technologies for nanolithography. Progress towards, and beyond, a 1000 W EUV source will continue to be supported by achievements in the fields of optics and photonics field by combining fundamental research with industrial innovation.

Data availability statement

No new data were created or analysed in this study.

Acknowledgments

ORCID iDs

O O Versolato ⬤ https://orcid.org/0000-0003-3852-5227
J Sheil ⬤ https://orcid.org/0000-0003-3393-9658
S Witte ⬤ https://orcid.org/0000-0002-1899-4395
W Ubachs ⬤ https://orcid.org/0000-0001-7840-3756
R Hoekstra ⬤ https://orcid.org/0000-0001-8632-3334

References

[1] Torretti F *et al* 2020 Prominent radiative contributions from multiply-excited states in laser-produced tin plasma for nanolithography *Nat. Commun.* **11** 2334
[2] Mack C A 2011 Fifty years of Moore's law *IEEE Trans. Semicond. Manuf.* **24** 202
[3] Waldrop M M 2016 The chips are down for Moore's law *Nature* **530** 144
[4] Moore G E 1998 Cramming more components onto integrated circuits *Proc. IEEE* **86** 82
[5] Moore G E 1975 Progress in digital integrated electronics *Proc. IEDM Tech. Dig.* **11** 11
[6] Moore G E 1995 Lithography and the future of Moore's law *Proc. SPIE* **2439** 2439
[7] van Schoot J *et al* 2018 The future of EUV lithography: continuing Moore's Law into the next decade *Proc. SPIE* **10583** 105830R
[8] Bajt S, Alameda J B, Barbee T W Jr, Clift W M, Folta J A, Kaufmann B and Spiller E A 2002 Improved reflectance and stability of Mo-Si multilayers *Opt. Eng.* **41** 1797
[9] Huang Q, Medvedev V, van de Kruijs R, Yakshin A, Louis E and Bijkerk F 2017 Spectral tailoring of nanoscale EUV and soft x-ray multilayer optics *Appl. Phys. Rev.* **4** 011104
[10] Meijer R A 2021 Tailored laser-droplet interaction: for target formation in extreme ultraviolet sources *PhD Thesis* Vrije Universiteit Amsterdam
[11] Versolato O O 2019 Physics of laser-driven tin plasma sources of EUV radiation for nanolithography *Plasma Sources Sci. Technol.* **28** 083001
[12] Bakshi V 2006 *EUV Sources for Lithography* (Bellingham, WA: SPIE Press) ch 11
[13] O'Sullivan G *et al* 2015 Spectroscopy of highly charged ions and its relevance to EUV and soft x-ray source development *J. Phys. B: At. Mol. Opt. Phys.* **48** 144025
[14] Reijers S A, Kurilovich D, Torretti F, Gelderblom H and Versolato O O 2018 Laser-to-droplet alignment sensitivity relevant for laser-produced plasma sources of extreme ultraviolet light *J. Appl. Phys.* **124** 013102
[15] Kurilovich D *et al* 2018 Expansion dynamics after laser-induced cavitation in liquid tin microdroplets *Phys. Rev. Appl.* **10** 054005
[16] Vinokhodov A, Krivokorytov M, Sidelnikov Y, Krivtsun V, Medvedev V, Bushuev V, Koshelev K, Glushkov D and Ellwi S 2016 Stable droplet generator for a high brightness laser produced plasma extreme ultraviolet source *Rev. Sci. Instrum.* **87** 103304
[17] Basko M M *et al* 2017 Fragmentation dynamics of liquid–metal droplets under ultra-short laser pulses *Laser Phys. Lett.* **14** 036001
[18] Krivokorytov M S, Vinokhodov A Y, Sidelnikov Y V, Krivtsun V M, Kompanets V O, Lash A A, Koshelev K N and Medvedev V V 2017 Cavitation and spallation in liquid metal droplets produced by subpicosecond pulsed laser radiation *Phys. Rev.* E **95** 031101
[19] Grigoryev S Y *et al* 2018 Expansion and fragmentation of a liquid-metal droplet by a short laser pulse *Phys. Rev. Appl.* **10** 064009
[20] Koukouvinis P, Kyriazis N and Gavaises M 2018 Smoothed particle hydrodynamics simulation of a laser pulse impact onto a liquid metal droplet *PLoS One* **13** 1
[21] de Faria Pinto T, Mathijssen J, Meijer R, Zhang H, Bayerle A, Kurilovich D, Versolato O O, Eikema K S and Witte S 2021 Cylindrically and non-cylindrically symmetric expansion dynamics of tin microdroplets after ultrashort laser pulse impact *Appl. Phys.* A **127** 1
[22] Kurilovich D, Klein A L, Torretti F, Lassise A, Hoekstra R, Ubachs W, Gelderblom H and Versolato O O 2016 Plasma propulsion of a metallic microdroplet and its deformation upon laser impact *Phys. Rev. Appl.* **6** 014018
[23] Kurilovich D *et al* 2018 Power-law scaling of plasma pressure on laser-ablated tin microdroplets *Phys. Plasmas* **25** 012709
[24] Hudgins D, Gambino N, Rollinger B and Abhari R 2016 Neutral cluster debris dynamics in droplet-based laser-produced plasma sources *J. Phys. D: Appl. Phys.* **49** 185205
[25] Klein A L, Bouwhuis W, Visser C W, Lhuissier H, Sun C, Snoeijer J H, Villermaux E, Lohse D and Gelderblom H 2015 Drop shaping by laser-pulse impact *Phys. Rev. Appl.* **3** 044018
[26] Gelderblom H, Lhuissier H, Klein A L, Bouwhuis W, Lohse D, Villermaux E and Snoeijer J H 2016 Drop deformation by laser-pulse impact *J. Fluid Mech.* **794** 676
[27] Liu B, Meijer R A, Hernandez-Rueda J, Kurilovich D, Mazzotta Z, Witte S and Versolato O O 2021 Laser-induced vaporization of a stretching sheet of liquid tin *J. Appl. Phys.* **129** 053302
[28] Liu B, Kurilovich D, Gelderblom H and Versolato O O 2020 Mass loss from a stretching semitransparent sheet of liquid tin *Phys. Rev. Appl.* **13** 024035
[29] Hassanein A, Sizyuk T, Sizyuk V and Harilal S 2011 Combined effects of pre-pulsing and target geometry on efficient EUV production from laser produced plasma experiments and modeling *Proc. SPIE* **7969** 79690D
[30] Freeman J, Harilal S and Hassanein A 2011 Enhancements of extreme ultraviolet emission using prepulsed Sn laser-produced plasmas for advanced lithography applications *J. Appl. Phys.* **110** 083303

[31] Freeman J R, Harilal S S, Hassanein A and Rice B 2013 Effect of prepulse laser wavelength on EUV emission from CO_2 reheated laser-produced Sn plasma *Appl. Phys.* A **110** 853

[32] Purvis M *et al* 2018 Industrialization of a robust EUV source for high-volume manufacturing and power scaling beyond 250W *Proc. SPIE* **10583** 1058327

[33] Langer S, Scott H, Galvin T, Link E, Regan B and Siders C W 2020 Simulations of laser driven EUV sources—the impact of laser wavelength *2020 Source Workshop* (EUV Litho) pp 1–25

[34] Behnke L *et al* 2021 Extreme ultraviolet light from a tin plasma driven by a 2-μm-wavelength laser *Opt. Express* **29** 4475

[35] Sheil J, Versolato O O, Scott H and Bakshi V 2021 Review of the 1st EUV source code comparison workshop (submitted)

[36] EUV Litho, Inc. (available at: https://euvlitho.com/)

[37] Liu K, Li Y, Zhang F and Fan M 2007 Transient thermal and structural deformation and its impact on optical performance of projection optics for extreme ultraviolet lithography *Jpn. J. Appl. Phys.* **46** 6568

[38] Yang G and Li Y 2012 Analysis and control of thermal and structural deformation of projection optics for 22-nm EUV lithography *Proc. SPIE* **8322** 83222V

[39] Svendsen W and O'Sullivan G 1994 Statistics and characteristics of XUV transition arrays from laser-produced plasmas of the elements tin through iodine *Phys. Rev.* A **50** 3710

[40] Torretti F, Schupp R, Kurilovich D, Bayerle A, Scheers J, Ubachs W, Hoekstra R and Versolato O O 2018 Short-wavelength out-of-band EUV emission from Sn laser-produced plasma *J. Phys. B: At. Mol. Opt. Phys.* **51** 045005

[41] Torretti F, Liu F, Bayraktar M, Scheers J, Bouza Z, Ubachs W, Hoekstra R and Versolato O 2019 Spectral characterization of an industrial EUV light source for nanolithography *J. Phys. D: Appl. Phys.* **53** 055204

[42] Benschop J, Banine V, Lok S and Loopstra E 2008 Extreme ultraviolet lithography: status and prospects *J. Vac. Sci. Technol.* B **26** 2204

[43] Banine V Y, Koshelev K N and Swinkels G H P M 2011 Physical processes in EUV sources for microlithography *J. Phys. D: Appl. Phys.* **44** 253001

[44] Giovannini A Z, Gambino N, Rollinger B and Abhari R S 2015 Angular ion species distribution in droplet-based laser-produced plasmas *J. Appl. Phys.* **117** 033302

[45] Deuzeman M J *et al* 2017 Ion distribution and ablation depth measurements of a fs-ps laser-irradiated solid tin target *J. Appl. Phys.* **121** 103301

[46] Stodolna A S *et al* 2018 Controlling ion kinetic energy distributions in laser produced plasma sources by means of a picosecond pulse pair *J. Appl. Phys.* **124** 053303

[47] Bayerle A *et al* 2018 Sn ion energy distributions of ns- and ps-laser produced plasmas *Plasma Sources Sci. Technol.* **27** 045001

[48] Basko M M, Novikov V G and Grushin A S 2015 On the structure of quasi-stationary laser ablation fronts in strongly radiating plasmas *Phys. Plasmas* **22** 053111

[49] Hernandez-Rueda J, Liu B, Hemminga D, Meijer R, Kurilovich D, Gelderblom H, Sheil J and Versolato O O 2021 Early-time hydrodynamic response of a tin droplet impacted by laser-produced plasma (unpublished)

[50] Cisneros G, Helman J S and Wagner C N J 1982 Dielectric function of liquid tin between 250 and 1100 °C *Phys. Rev.* B **25** 4248

[51] Culick F E C 1960 Comments on a ruptured soap film *J. Appl. Phys.* **31** 1128

[52] Meijer R A, Kurilovich D, Liu B, Mazzotta Z, Hernandez-Rueda J, Versolato O O and Witte S 2021 Laser ablation threshold of liquid tin microdroplets (unpublished)

[53] Shevelko A P, Shmaenok L A, Churilov S S, Bastiaensen R K F J and Bijkerk F 1998 Extreme ultraviolet spectroscopy of a laser plasma source for lithography *Phys. Scr.* **57** 276

[54] Kauffman R L, Phillion D W and Spitzer R C 1993 X-ray production ~13 nm from laser-produced plasmas for projection x-ray lithography applications *Appl. Opt.* **32** 6897

[55] Hayden P, Cummings A, Murphy N, O'Sullivan G, Sheridan P, White J and Dunne P 2006 13.5 nm extreme ultraviolet emission from tin based laser produced plasma sources *J. Appl. Phys.* **99** 093302

[56] Harilal S S, Shay B O, Tillack M S, Tao Y, Paguio R, Nikroo A and Back C A 2006 Spectral control of emissions from tin doped targets for extreme ultraviolet lithography *J. Appl. Phys.* **39** 484

[57] Tao Y, Harilal S, Tillack M, Sequoia K, O'Shay B and Najmabadi F 2006 Effect of focal spot size on in-band 13.5 nm extreme ultraviolet emission from laser-produced Sn plasma *Opt. Lett.* **31** 2492

[58] Coons R W, Harilal S S, Campos D and Hassanein A 2010 Analysis of atomic and ion debris features of laser-produced Sn and Li plasmas *J. Appl. Phys.* **108** 063306

[59] Campos D, Harilal S and Hassanein A 2010 The effect of laser wavelength on emission and particle dynamics of Sn plasma *J. Appl. Phys.* **108** 113305

[60] George S A, Silfvast W T, Takenoshita K, Bernath R T, Koay C-S, Shimkaveg G and Richardson M C 2007 Comparative extreme ultraviolet emission measurements for lithium and tin laser plasmas *Opt. Lett.* **32** 997

[61] Schupp R *et al* 2019 Efficient generation of extreme ultraviolet light from Nd:YAG-driven microdroplet-tin plasma *Phys. Rev. Appl.* **12** 014010

[62] Shimada Y *et al* 2005 Characterization of extreme ultraviolet emission from laser-produced spherical tin plasma generated with multiple laser beams *Appl. Phys. Lett.* **86** 051501

[63] Tanaka H, Matsumoto A, Akinaga K, Takahashi A and Okada T 2005 Comparative study on emission characteristics of extreme ultraviolet radiation from CO_2 and Nd:YAG laser-produced tin plasmas *Appl. Phys. Lett.* **87** 041503

[64] Harilal S S, Coons R W, Hough P and Hassanein A 2009 Influence of spot size on extreme ultraviolet efficiency of laser-produced Sn plasmas *Appl. Phys. Lett.* **95** 221501

[65] Harilal S, Sizyuk T, Hassanein A, Campos D, Hough P and Sizyuk V 2011 The effect of excitation wavelength on dynamics of laser-produced tin plasma *J. Appl. Phys.* **109** 063306

[66] Ueno Y, Soumagne G, Sumitani A, Endo A and Higashiguchi T 2007 Enhancement of extreme ultraviolet emission from a CO_2 laser-produced Sn plasma using a cavity target *Appl. Phys. Lett.* **91** 231501

[67] Amano R *et al* 2018 Influence of short pulse duration of carbon dioxide lasers on extreme ultraviolet emission from laser-produced plasmas *Jpn. J. Appl. Phys.* **57** 070311

[68] Yamaura M *et al* 2005 Characterization of extreme ultraviolet emission using the fourth harmonic of a Nd:YAG laser *Appl. Phys. Lett.* **86** 181107

[69] Mizoguchi H *et al* 2020 Challenge of >300W high power LPP-EUV source with long collector mirror lifetime for semiconductor HVM *Proc. SPIE* **11323** 225–38

[70] Fomenkov I *et al* 2017 Light sources for high-volume manufacturing EUV lithography: technology, performance and power scaling *Adv. Opt. Technol.* **6** 173

[71] Freeman J R, Harilal S S, Verhoff B, Hassanein A and Rice B 2012 Laser wavelength dependence on angular emission dynamics of Nd: YAG laser-produced Sn plasmas *Plasma Sources Sci. Technol.* **21** 055003

[72] Schupp R, Behnke L, Sheil J, Bouza Z, Bayraktar M, Ubachs W, Hoekstra R and Versolato O O 2021 Characterization of 1-and 2- μm-wavelength laser-produced microdroplet-tin plasma for generating extreme-ultraviolet light *Phys. Rev. Res.* **3** 013294

[73] Bakshi V 2018 *EUV Lithography* 2nd edn (Bellingham, WA: SPIE Press)

[74] Siders C W, Erlandson A C, Galvin T C, Frank H, Langer S, Reagan B A, Scott H, Sistrunk E F and Spinka T M 2019 Efficient high power laser drivers for next-generation high power EUV sources *2019 Source Workshop* (EUV Litho) pp 1–23

[75] Schupp R *et al* 2019 Radiation transport and scaling of optical depth in Nd:YAG laser-produced microdroplet-tin plasma *Appl. Phys. Lett.* **115** 124101

[76] Fujioka S *et al* 2005 Opacity effect on extreme ultraviolet radiation from laser-produced tin plasmas *Phys. Rev. Lett.* **95** 235004

[77] White J, Dunne P, Hayden P, O'Reilly F and O'Sullivan G 2007 Optimizing 13.5 nm laser-produced tin plasma emission as a function of laser wavelength *Appl. Phys. Lett.* **90** 181502

[78] Schupp R *et al* 2021 Characterization of angularly resolved EUV emission from 2-μm-wavelength laser-driven Sn plasmas using preformed liquid disk targets *J. Phys. D: Appl. Phys.* **54** 365103

[79] Wagner C and Harned N 2010 Lithography gets extreme *Nat. Photon.* **4** 24

[80] Kawasuji Y *et al* 2017 Key components technology update of the 250W high-power LPP-EUV light source *Proc. SPIE* **10143** 101432G

[81] Azarov V I and Joshi Y N 1993 Analysis of the $4d^7$-$4d^6 5p$ transition array of the eighth spectrum of tin: Sn VIII *J. Phys. B: At. Mol. Opt. Phys.* **26** 3495

[82] Churilov S S and Ryabtsev A N 2006 Analyses of the Sn IX–Sn XII spectra in the EUV region *Phys. Scr.* **73** 614

[83] Churilov S S and Ryabtsev A N 2006 Analysis of the 4p 64d 7-(4p 64d 64f + 4p 54d 8) transitions in the Sn VIII spectrum *Opt. Spectrosc.* **100** 660

[84] Churilov S S and Ryabtsev A N 2006 Analysis of the spectra of in XII–XIV and Sn XIII–XV in the far-VUV region *Opt. Spectrosc.* **101** 169

[85] Ryabtsev A N, Kononov E Y and Churilov S S 2008 Spectra of rubidium-like Pd X-Sn XIV ions *Opt. Spectrosc.* **105** 844

[86] Tolstikhina I Y, Churilov S S, Ryabtsev A N and Koshelev K N 2006 Atomic tin data *EUV Sources for Lithography* ed V Bakshi (Bellingham, WA: SPIE Press) ch 4, pp 113–48

[87] Ohashi H, Suda S, Tanuma H, Fujioka S, Nishimura H, Sasaki A and Nishihara K 2010 EUV emission spectra in collisions of multiply charged Sn ions with He and Xe *J. Phys. B: At. Mol. Opt. Phys.* **43** 065204

[88] Windberger A *et al* 2016 Analysis of the fine structure of Sn^{11+}–Sn^{14+} ions by optical spectroscopy in an electron-beam ion trap *Phys. Rev.* A **94** 012506

[89] Colgan J, Kilcrease D, Abdallah J, Sherrill M, Fontes C, Hakel P and Armstrong G 2017 Atomic structure considerations for the low-temperature opacity of Sn *High Energy Density Phys.* **23** 133

[90] Torretti F *et al* 2017 Optical spectroscopy of complex open-4 *d*-shell ions Sn^{7+} − Sn^{10+} *Phys. Rev.* A **95** 042503

[91] Bauche J, Bauche-Arnoult C and Klapisch M 1988 Transition arrays in the spectra of ionized atoms *Adv. Atom. Mol. Phys.* **23** 131

[92] Sheil J, Versolato O O, Neukirch A J and Colgan J 2021 Multiply-excited states and their contribution to opacity in CO_2 laser-driven tin-plasma conditions *J. Phys. B: At. Mol. Opt. Phys.* **54** 035002

[93] Busquet M 1993 Radiation-dependent ionization model for laser-created plasmas *Phys. Fluids* B **5** 4191

[94] Scheers J *et al* 2020 EUV spectroscopy of highly charged Sn^{13+} − Sn^{15+} ions in an electron-beam ion trap *Phys. Rev.* A **101** 062511

[95] Bouza Z *et al* 2020 EUV spectroscopy of Sn^{5+}–Sn^{10+} ions in an electron beam ion trap and laser-produced plasmas *J. Phys. B: At. Mol. Opt. Phys.* **53** 195001

[96] Bouza Z *et al* 2021 The spectrum of a 1-μm-wavelength-driven tin microdroplet laser-produced plasma source in the 5.5–265.5 nm wavelength range *AIP Adv.* **11** 125003

[97] Byers J, Bouza Z, Versolato O O and Bayraktar M 2022 Imaging transmission grating spectrometer using a tapered fresnel zone plate (in preparation)

[98] Scheers J *et al* 2018 Energy-level structure of Sn^{3+} ions *Phys. Rev.* A **98** 062503

[99] Scheers J, Schupp R, Meijer R, Ubachs W, Hoekstra R and Versolato O O 2020 Time-and space-resolved optical Stark spectroscopy in the afterglow of laser-produced tin-droplet plasma *Phys. Rev.* E **102** 013204

[100] Rai S, Bijlsma K, Koeleman S, Tjepkema O, Noordam A, Jonkman H, Versolato O and Hoekstra R 2020 Single-collision scattering of keV-energy Kr ions off a polycrystalline Cu surface *Nucl. Instrum. Methods Phys. Res.* B **482** 58

[101] Rai S, Deuzemann M, Noordam W, Holleman E, Versolato O O and Hoekstra R 2020 The missing single-scattering peak in tin ion collisions on Mo and Ru targets *J. Phys.: Conf. Ser.* **1412** 202019

[102] Ziegler J, Biersack J and Littmark U 1985 The stopping and range of ions in matter *Treatise on Heavy-Ion Science* (New York: Pergamon) pp 93–129

[103] Hoekstra R, De Heer F J and Morgenstern R 1991 State-selective electron capture in collisions of He^{2+} with H *J. Phys. B: At. Mol. Opt. Phys.* **24** 4025

[104] Folkerts H O, Bliek F W, De Jong M C, Hoekstra R and Morgenstern R 1997 Dissociation of CO induced by ions: I. Fragmentation and kinetic energy release spectra *J. Phys. B: At. Mol. Opt. Phys.* **30** 5833

[105] Mora P 2003 Plasma expansion into a vacuum *Phys. Rev. Lett.* **90** 185002

[106] Hemminga D J, Poirier L, Basko M M, Hoekstra R, Ubachs W, Versolato O O and Sheil J 2021 High-energy ions from Nd: YAG laser ablation of tin microdroplets: comparison between experiment and a single-fluid hydrodynamic model *Plasma Sources Sci. Technol.* **30** 105006

[107] Poirier L, Ubachs W, Versolato O, Sheil J and Hoekstra R 2021 Cross-calibration of a combined electrostatic and time-of-flight analyzer for energy- and charge-state-resolved spectrometry of tin laser-produced plasma (unpublished)

[108] van de Kerkhof M, Liu F, Meeuwissen M, Zhang X, Bayraktar M, de Kruif R and Davydova N 2020 High-power EUV lithography: spectral purity and imaging performance *J. Micro Nanolithogr. MEMS MOEMS* **19** 033801

[109] Mazzotta Z, Mathijssen J, Eikema K, Versolato O and Witte S 2021 TI-REX: a tunable infrared laser for experiments in nanolithography *Conf. on Lasers and Electro-Optics* (Optical Society of America) p cd_p_28